Journal of Physics B:
Atomic, Molecular and
Optical Physics

Circularly polarized RABBITT on atomic shells with large orbital momentum

OPEN ACCESS
IOP Publishing
Journal of Physics B: Atomic, Molecular and Optical Physics
J. Phys. B: At. Mol. Opt. Phys. **58** (2025) 045601 (9pp)
https://doi.org/10.1088/1361-6455/ada98b

Circularly polarized RABBITT on atomic shells with large orbital momentum

Anatoli S Kheifets

Fundamental and Theoretical Physics, Research School of Physics, The Australian National University, Canberra 2601, Australia

E-mail: a.kheifets@anu.edu.au

Received 14 November 2024, revised 22 December 2024
Accepted for publication 12 January 2025
Published 4 February 2025

Abstract

In light atoms, the technique of Reconstruction of Attosecond Bursts by Interference of Two-Photon Transitions (RABBITT), driven by circularly polarized radiation, enables a complete retrieval of ionization amplitudes in the XUV+IR regime, including their relative phases (Kheifets 2024 *Phys. Rev. Res.* **6** L012002). In this work, we extend this method to heavier atoms by conducting numerical simulations of circularly polarized RABBITT on the Kr $3d$ and Xe $4d$ atomic shells. The XUV ionization dynamics in these atoms differ markedly due to the presence of a 'giant' shape resonance in the $4d \rightarrow Ef$ ionization channel of Xe, a feature absent in Kr. Nevertheless, when an IR photon is added to the XUV ionization, the results for Kr and Xe are surprisingly similar, with the ratio of absorption/emission matrix elements and their relative phases remaining close in value. Moreover, these ratios and phases show minimal variation even when the Xe atom is encapsulated within a C_{60} fullerene cage. In search for the Cooper-like minimum in the IR absorption amplitude ratios predicted in Ji *et al* (2024 *J. Phys.* B **57** 235601), we extend our investigation to the Ce $4f$ shell where this minimum is indeed present.

Keywords: RABBITT, atomic ionization, ultrafast science, Attosecond science

1. Introduction

Two-photon interferometric techniques, such as Reconstruction of Attosecond Beating by Interference of Two-Photon Transitions (RABBITT), have found extensive applications in attosecond science following the pioneering work [1]. In the RABBITT technique, a comb of ionizing XUV harmonics is complemented by the absorption or emission of an IR photon. The arrival times of the XUV and IR photons are precisely synchronized, while their relative delay, Δ, is varied. This IR photon absorption/emission creates sidebands (SBs) positioned between the primary XUV absorption peaks. The population of these sidebands oscillates at twice the IR photon frequency as Δ is varied:

$$S_{\rm SB}(\Delta) = A + B\cos[2\omega\Delta - C] \quad , \quad C = 2\omega\tau_a \quad , \quad \tau_a = \tau_W + \tau_{cc} \, . \tag{1}$$

Here A, B are the RABBITT magnitudes parameters and C is its phase. The latter is conveniently linked with the atomic time delay τ_a composed of the Wigner time delay τ_W and the continuum-continuum (CC) component τ_{cc} [2].

In most RABBITT applications, the XUV and IR pulses are co-linearly polarized. More recently, RABBITT with circularly polarized XUV and IR radiation, either co- or counter-rotated, has been suggested [3] and then successfully implemented [4–6]. The strong helicity dependence in circular RABBITT (*c*RABBITT) enables the reconstruction of the magnitude ratio and phase difference of the two-photon XUV+IR ionization amplitudes [7]. Depending on the angular momentum projection of the initial target orbital, the co- and counter-rotating XUV and IR pulses create final continuum

states that contain either a single or dual partial waves. The interference between these different continuum states in the IR absorption (+) and emission (–) processes generates a specific combination of spherical harmonics. This combination can be disentangled from the RABBIT phase $C(\theta)$ known as a function of the photoelectron emission angle θ. In this way, the angular-independent modulus ratio and relative phase

$$R^{\pm} = \left| T^{\pm}_{\ell\to\ell-1}/T^{\pm}_{\ell\to\ell+1} \right| \ , \ \Delta\Phi^{\pm} = \arg\left\{ T^{\pm}_{\ell\to\ell-1}/T^{\pm}_{\ell\to\ell+1} \right\} \tag{2}$$

can be retrieved from a numerically simulated or experimentally measured *c*RABBITT process.

The moduli ratios $R^{\pm}$ are of particular interest because of the recently formulated Fano propensity rule in the two-photon ionization processes [8]. By virtue of this rule, the angular momentum is preferably increased or decreased in the IR photon absorption/emission processes, respectively. This implies the inequalities $R^{+} < 1$ and $R^{-} > 1$. These inequalities have indeed been confirmed by numerical *c*RABBITT simulations in He 1*s* and Ar 3*p* shells. In the weak IR field regime, the RABBIT process is well described by the soft photon approximation (SPA) [9]. Within the SPA, the combined two-photon amplitudes are factorized into the product of separate XUV and IR parts and it is the IR part that is fully responsible for the $\ell \to \ell \pm 1$ ratios and phases. The IR driven ratios $R^{\pm}$ can be conveniently analyzed within the quasiclassical approximation [10, 11]. These analytical predictions provide a rigid test for numerical *c*RABBITT simulations. Not only that, at a sufficiently high photon frequency, large orbital momentum of the target and low photoelectron energy, a departure from the Fano propensity rule is predicted in [11] with the counter-rotating polarization being able to produce $R^{+} > 1$. At the photoelectron energies in between the two regimes of $R^{+} < 1$ and $R^{+} > 1$, the absorption ratio passes through a characteristic Cooper-like minimum.

These recent theoretical advances motivate us to extend the evaluation of *c*RABBITT amplitudes, previously conducted in He and Ar [7], to heavier atomic targets such as Kr 3*d* and Xe 4*d*. While the He ratios align well with predictions from the hydrogenic model, the ratios for Ar, Kr, and Xe are compared against a recently developed analytical model [11]. Agreement across all these targets is very satisfactory. Comparing the results for Kr 3*d* and Xe 4*d* reveals a minimal dependence of $R^{\pm}$ and $\Delta\Phi^{\pm}$ on the specific target orbital. Moreover, encasing the Xe atom in a C_{60} fullerene cage does not significantly alter the ratios, even in the presence of confinement resonances. Such resonances occur when the photoelectron de Broglie wavelength is resonant with the size of the cage. The relative phase, however, shows greater sensitivity, exhibiting some oscillatory behavior. These findings support the general assumption that IR photon dressing occurs at sufficiently large distances and are minimally affected by the atomic electronic structure and the ionic potential of the target. At these distances, the ionic potential is asymptotically hydrogenic. Finally, in the search of the Cooper-like minimum in R^{+}, we extend our investigation to the 4*f* shell of the cerium atom where this minimum is indeed present.

The remainder of this paper is organized as follows. In section 2, we describe our numerical technique, which is based on solving the time-dependent Schrödinger equation (TDSE) under the influence of circularly polarized XUV and IR pulses. In section 3, we outline the lowest-order perturbation theory (LOPT) framework, which provides an analytical interpretation of our results through angular momentum algebra. Our numerical results are presented and analyzed in section 4. In section 4.1, we validate our results by comparing them with photoionization cross-sections and angular anisotropy β parameters from previous synchrotron studies. In section 4.2, we examine the angular dependence of the *c*RABBITT phase to determine the amplitude ratios and relative phases. Finally, we summarize our main findings and discuss future directions for this research in section 5.

2. TDSE formalism

As in our earlier applications [12–14], we solve numerically the one-electron TDSE in the single active electron approximation

$$i\,\partial\Psi(\boldsymbol{r})/\partial t = \left[\hat{H}_{\rm atom} + \hat{H}_{\rm int}(t)\right]\Psi(\boldsymbol{r}) \ . \tag{3}$$

The electromagnetic interaction is written in the velocity gauge

$$\hat{H}_{\rm int}(t) = \boldsymbol{A}(t)\cdot\hat{\boldsymbol{p}} \ , \ \boldsymbol{A}(t) = -\int_0^t \boldsymbol{E}(t')\,{\rm d}t' \ . \tag{4}$$

The TDSE (3) is driven by the vector potential $\boldsymbol{A}(t)$ which includes both the XUV and IR fields. The XUV field is represented by an attosecond pulse train (APT) composed of eleven equally spaced pulseletts of the opposite polarity:

$$A_x(t) = \sum_{n=-5}^{5} (-1)^n A_n \exp\left(-2\ln 2\frac{(t-nT/2)^2}{\tau_x^2}\right) \times \cos\left[\omega_x(t-nT/2)\right] \ . \tag{5}$$

Here

$$A_n = A_0 \exp\left(-2\ln 2\frac{(nT/2)^2}{\tau_T^2}\right) .$$

and A_0 is the vector potential peak value while $T = 2\pi/\omega$ is the period of the IR field. The XUV central frequency is $\omega_x = 60$ eV for Xe 4d and 79 eV for Kr 3d while the time constants τ_x, τ_T are chosen to span a sufficient number of harmonics in the range of photon frequencies of interest for a given atom. The IR pulse with the wavelength of 780 nm has a cosine squared envelope shifted from the center of the APT by a variable delay Δ. The latter is incremented in seven steps by 10 a.u. each. The XUV and IR intensities are kept

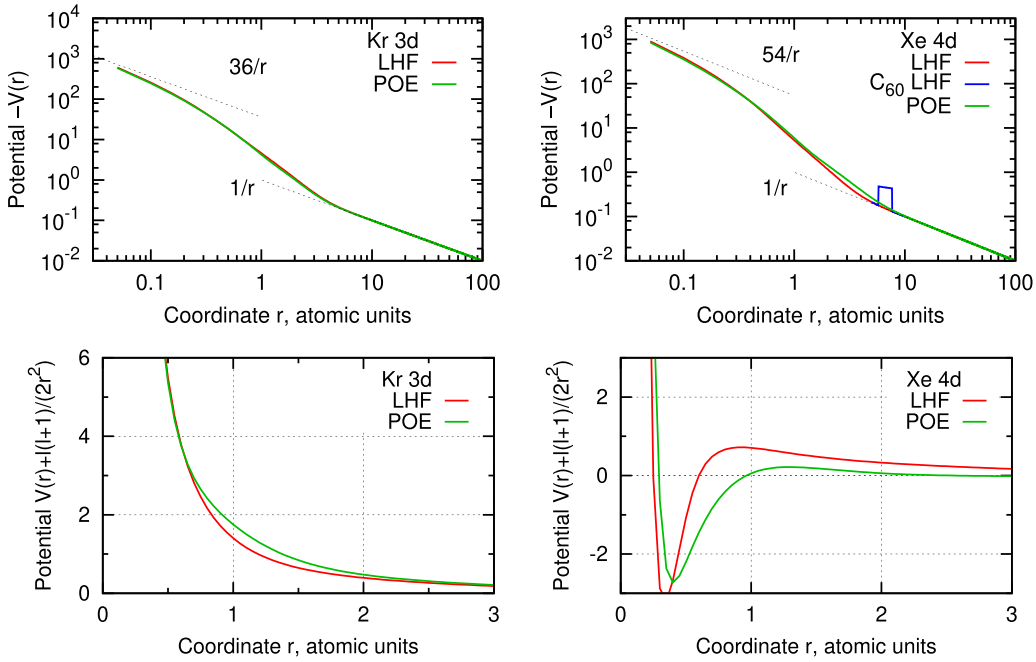

Figure 1. One-electron effective potentials in Kr 3*d* (left) and Xe 4*d* (right). The top panels show $-V(r)$ in the logarithmic scale where the short-range $(Z-1)/r$ and the long range $1/r$ asymptotics are displayed. In the case of Xe 4*d*, the C_{60} cage potential is also shown. The bottom panels exhibit the one-electron potential augmented by the centrifugal term $\ell(\ell+1)/(2r^2)$ to visualize the formation of the potential well in Xe 4*d* and lack of thereof in Kr 3*d*. Results with the POE and LHF potentials are shown to demonstrate formation of the potential well for Xe.

low in the $\times 10^{10}$ W cm^{-2} range to retain the ionization process within the LOPT domain. The choice of the one-electron potential entering $\hat{H}_{\rm atom}$ is described in [13]. As in [14], an attractive spherical square well potential is introduced to represent the C_{60} cage. These potentials are illustrated graphically in figure 1

The TDSE (3) is solved numerically by the spherical-coordinate implicit derivatives (SCID) computer code [15]. The photoelectron momentum distribution (PMD) is obtained using the time-dependent surface flux (t-SURF) method [16, 17]. The PMD is expressed as the projection of the time-dependent wave function after the end of propagation on the basis of scattering states,

$$P_{nlm}(\boldsymbol{k}) = \left| \langle \varphi_{\boldsymbol{k}}(r) | \Psi_{nlm}(\boldsymbol{r}, t \to \infty) | \rangle \right|^2 . \tag{6}$$

Here the indexes n, l, m denote the initial atomic orbital. The photoelectron momentum $\boldsymbol{k}$ is defined in the Cartesian frame in which the $\hat{z}$ axis is aligned with the light propagation direction and the (x, y) plane contains the vector potentials of both the XUV and IR fields. Projection of the PMD on the (x, z) plane serves to determine the angular profile of a given spectral feature:

$$S_N(\theta) = P_{nlm}(k_x, k_y = 0, k_z) \quad , \ \theta = \tan^{-1}(k_z/k_x) ,$$
$$E = \left(k_x^2 + k_z^2\right)/2 = N\omega - I_p . \tag{7}$$

Here E is the photoelectron energy while $N = 2q$ for a sideband and $N = 2q \pm 1$ for a primary harmonic peak. In equation (9) the bound state indices nlm are assumed on $S_N(\theta)$ but dropped for brevity and I_p is the ionization potential of the target orbital. The k-grid is sufficiently dense to specify the angle θ with a 2° increment.

Present computations are fairly time consuming because the TDSE should be propagated to a fairly large times on a fine grid before the PMD could be extracted at sufficiently large distances away from the nucleus. Each set of CO or CR calculations with several increments of the XUV/IR delay takes about 10^4 CPU hours of the Gadi supercomputer [18].

Very considerable efforts have been made to ensure a full numerical convergence of the TDSE results. More specifically, the radial, angular and momentum grids were thoroughly tested as well as the overall propagation time and the time increment at each propagation step.

3. Lowest order perturbation (LOPT) formalism

Within the LOPT theory, the two-photon amplitude of the XUV absorption and the IR absorption/emission $(\pm)$ is given by the following expression [2, 19]:

$$\mathcal{M}_m^{\pm}(\boldsymbol{k}) \propto \mathcal{E}_\Omega \mathcal{E}_\omega \sum_{\lambda=l\pm1} \sum_{L=\lambda\pm1} \sum_{|M|\leqslant L; |\mu|\leqslant\lambda} (-i)^L e^{i\eta_L} Y_{LM}\left(\hat{k}\right)$$
$$\times \sum\!\!\!\!\!\!\int d^3\kappa \, \frac{\langle R_{kL}|r|R_{\kappa\lambda}\rangle \langle R_{\kappa\lambda}|r|R_{ln}\rangle}{E_i + \Omega^{\pm} - \kappa^2/2 - i\gamma} \langle Y_{LM}|Y_{1m_2}|Y_{\lambda\mu}\rangle$$
$$\times \langle Y_{\lambda\mu}|Y_{1m_1}|Y_{lm}\rangle . \tag{8}$$

Here $\mathcal{E}_\Omega, \mathcal{E}_\omega$ are the spectral contents of the XUV and IR fields, respectively, while $\langle nl|$, $\langle \kappa\lambda|$ and $\langle kL|$ are the initial, intermediate and final electron states defined by their linear and angular

momenta. The linear polarization (the LIN case) corresponds to $m_1 = m_2 = 0$ whereas for the circular polarization $m_1 = 1$ and $m_2 = \pm 1$ in the co- and counter-rotating (CO/CR) cases, respectively.

While the radial part of equation (3) is generally not separable into the XUV and IR components, such a separation can be conducted in the angular part containing the following spherical harmonics:

$$\mathcal{M}^{\pm}_{m_i}(\boldsymbol{k}) \propto \underline{T_L \times Y_{LM}\left(\hat{k}\right) \langle Y_{LM}|Y_{1m}|Y_{\lambda\mu}\rangle} \langle Y_{\lambda\mu}|Y_{1m_1}|Y_{l_i m_i}\rangle \,. \quad (9)$$

The underlined expression defines the angular momentum dependence in the final continuum while the remainder is common for the two $L = \lambda \pm 1$ continuum channels. Here the radial part is absorbed into T_L with the rest of the indices dropped for brevity of notations. The underlined angular part has the following structure for the d and f initial states with various angular momentum projections:

$$\begin{aligned}
l_i = 2 \quad m_i = 1 \quad &\propto \quad -T_2 + \frac{3}{10}\bar{P}^1_4(\cos\theta)\; T_4 \quad \bar{P}^1_4 = \frac{P^1_4}{P^1_2} = \frac{5}{6}\left(-3 + 7\cos^2\theta\right) \\
m_i = 2 \quad &\propto \quad -T_2 + \frac{1}{15}\bar{P}^2_4(\cos\theta)\; T_4 \quad \bar{P}^2_4 = \frac{P^2_4}{P^2_2} = \frac{5}{2}\left(-1 + 7\cos^2\theta\right) \\
l_i = 3 \quad m_i = 3 \quad &\propto \quad -T_3 + \frac{1}{28}\bar{P}^3_5(\cos\theta)\; T_5 \quad \bar{P}^3_5 = \frac{P^3_5}{P^3_3} = \frac{7}{2}\left(-1 + 9\cos^2\theta\right)
\end{aligned} \quad . \quad (10)$$

Here we tabulated only those angular momentum projections which correspond to a single partial wave continuum. It is those projections that we will be using to deduce the amplitude ratios and relative phases of equation (2). Equation (10) defines the angular dependence of the RABBITT phase. For the d initial state, it is

$$\begin{aligned}
C^{\mathrm{CR/CO}}_{m=1} &= \arg\left[T^{+*}_4 T^{-}_4\right] + \arg\left[\frac{3}{10}\bar{P}^2_4(\cos\theta) - \frac{T^{\pm}_2}{T^{\pm}_4}\right] \\
C^{\mathrm{CR/CO}}_{m=2} &= \arg\left[T^{+*}_4 T^{-}_4\right] + \arg\left[\frac{1}{15}\bar{P}^2_4(\cos\theta) - \frac{T^{\pm}_2}{T^{\pm}_4}\right] .
\end{aligned} \quad (11)$$

The analogous expressions for the f initial state are

$$C^{\mathrm{CR/CO}}_{m=3} = \arg\left[T^{+*}_5 T^{-}_5\right] + \arg\left[\frac{1}{28}\bar{P}^3_5(\cos\theta) - \frac{T^{\pm}_3}{T^{\pm}_5}\right] . \quad (12)$$

In equations (10) and (11), the azimuthal angle θ is counted from the common propagation direction of the XUV/IR light and the polar angle ϕ is assumed to be zero. By examining equations (11) and (12), we observe that the CR phase depends on the $R^+ < 1$ ratio whereas its CO counterpart allows to recover the $R^- > 1$ ratio. This ratio and phase recovery is conducted by fitting numerical TDSE results with the corresponding analytic expressions. Said fitting is conducted with a nonlinear least-squares Marquardt–Levenberg algorithm [20].

4. Numerical results

4.1. XUV photoionization

Single-photon XUV ionization of Kr $3d$ and Xe $4d$ is firmly established in earlier synchrotron studies. These sub-valent atomic shells are well separated from the core and the valence shell and their single-photon ionization is largely free from inter-shell correlation. This allows to represent the XUV ionization process by an effective one-electron potential which can be localized for the purpose of its deployment in the TDSE modeling.

In our previous angular resolved RABBITT simulations in valence shells of noble gas atoms [13], we employed the parameterized optimized effective (POE) potential from [22]. While this potential is well suited for the Kr $3d$ shell, its utilization in Xe $4d$ calculations [14] needs to be re-examined. This particular sensitivity of Xe $4d$ ionization to the effective one-electron potential can be understood from figure 1. This figure exhibits the Kr $3d$ (left) and Xe $4d$ (right) effective potentials in the asymptotic regions (top) and at middle distances (bottom) where the centrifugal term is added to illustrate the formation of the potential well in Xe and lack of thereof in Kr. The localized Hartree–Fock potential (LHF) is employed both for Kr $3d$ and Xe $4d$. This potential is constructed from the $3d \to Ef$ continuous orbitals as prescribed in [23]. The LHF potential takes the form

$$\begin{aligned}
V(r) &= -\frac{Q(r)}{r} \quad , \\
Q(r) &= b\exp(-r) + (Z - 1 - b)\exp(-ar) + 1
\end{aligned} \quad (13)$$

with $Z = 36, a = 4.44, b = 8.94$ for Kr and $Z = 54, a = 4.16, b = 9.84$ for Xe. The difference between the POE and LHF potentials is very manifest in Xe where the formation of the potential well shown in the bottom right panel of figure 1. This well is much narrower and the potential barrier is higher with the LHF potential in comparison with the POE one.

We can judge on the accuracy of the effective one-electron potentials by comparing the main characteristics of the XUV photoionization deduced from TDSE with time-independent studies. This comparison is most straightforward for linearly

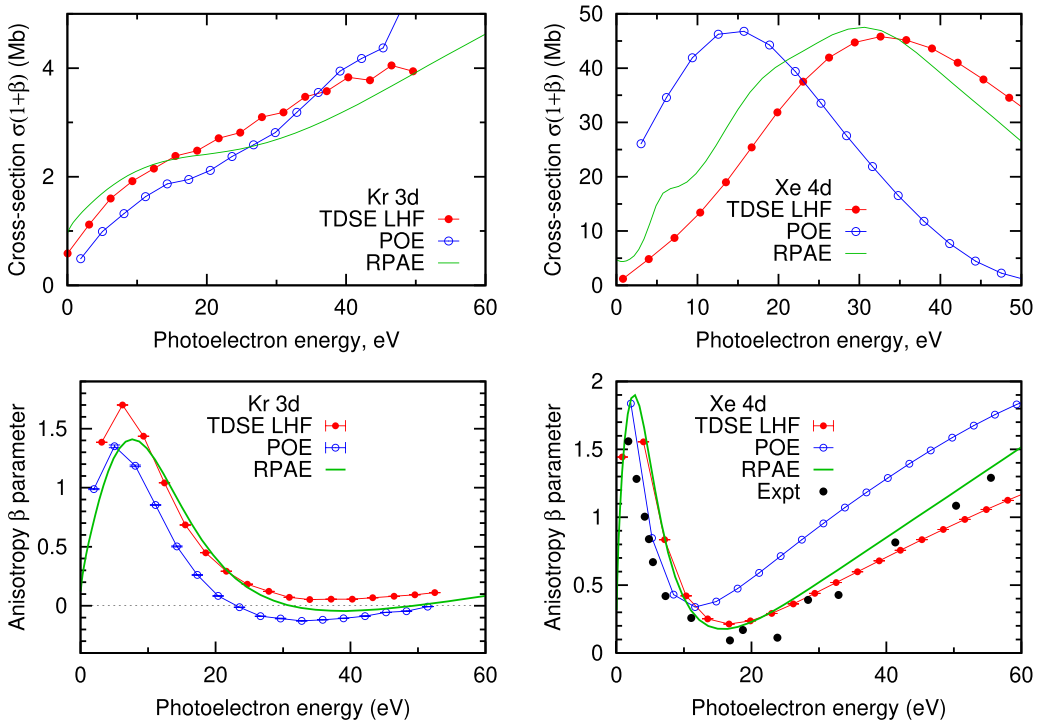

Figure 2. Photoionization cross-section in the polarization direction (top) and angular anisotropy β parameter (bottom) in Kr $3d$ (left) and Xe $4d$ (right). The values extracted from the primary harmonic peaks marked as TDSE are compared with the corresponding RPAE results. Experimental data for the β parameter in Xe are from [21].

polarized XUV radiation. In this case, the height of the primary harmonic peaks normalized to the spectral content of the XUV radiation is proportional to the corresponding photoionization cross-section in the forward direction $S_{2q+1}/\mathcal{E}_\Omega \propto \sigma(E) \times (1+\beta(E))$. In addition, the angular variation $S_{2q+1}(\theta) \propto 1 + \beta(E)P_2(\cos\theta)$ defines the angular anisotropy β parameter [14].

In figure 2 we compare the photoionization cross-sections (top) and the β-parameters (bottom) deduced from the TDSE with the time-independent calculations using the random phase approximation with exchange (RPAE). The latter approximation is well established against a large body of experimental data [24]. While agreement between the TDSE and RPAE for Kr $3d$ is fair with both potentials, the TDSE results with the POE potential are manifestly off for Xe $4d$. In the meantime, the LHF potential largely removes this disagreement.

4.2. Angular dependent cRABBITT phase

The cRABBITT magnitude and phase parameters are found by using the cosine fit of equation (1) into the SB oscillation signal in a given direction. In figure 3 we exhibit the angular dependent cRABBITT phase $C(\theta)$ as a function of the photoelectron emission angle θ. The angular range of $90^\circ \le \theta \le 180^\circ$ is only displayed which corresponds to the top hemisphere of the photoelectron emission. The lower hemisphere is not shown as the photoelectron angular distribution is symmetric relative to the equatorial xy plane. The top row of panels in the figure displays the cRABBITT phase for the lowest SB40–44 in Xe $4d$ whereas the bottom row visualizes the SB66–70 in Kr $3d$. The angular momentum projection of the target orbital is fixed at $M = 1, 2$ as it is those projections that allow for an unambiguous extraction of the ratios and relative phases according to equation (10). The two sets of data are displayed corresponding to the CO/CR polarization of the XUV and IR radiation.

The raw C-values extracted from the time variation of the cRABBITT signal (1) are shown with error bars which indicate the accuracy of the cosine fit with equation (1). The raw C-values are fitted with the corresponding analytic expressions of equation (11). The fitted values are shown by the solid lines of matching color. We notice a gradual convergence of the cRABBITT phase near $\theta = 90^\circ$ as the SB order grows.

4.3. Amplitude ratios and relative phases

The angular fit with equations (11) and (12) is used to extract the absolute ratios $R^\pm$ and their relative phases $\Delta\Phi$. We start analyzing these results in figure 4 where we display the T_2/T_4 ratios for the Kr $3d$ (right) in comparison with the T_1/T_3 ratios for Ar $3p$ from [7] (left). The Ar data were analyzed previously where agreement was found poor with a hydrogenic model of [25]. Predictions of this model are exhibited by the dotted lines in the top left panel. In comparison, a more advanced analytic model of [11] provides a much better guidance to our numerical data both for Ar $3p$ and Kr $3d$. The relative phase predictions of this model are also rather close to our data except

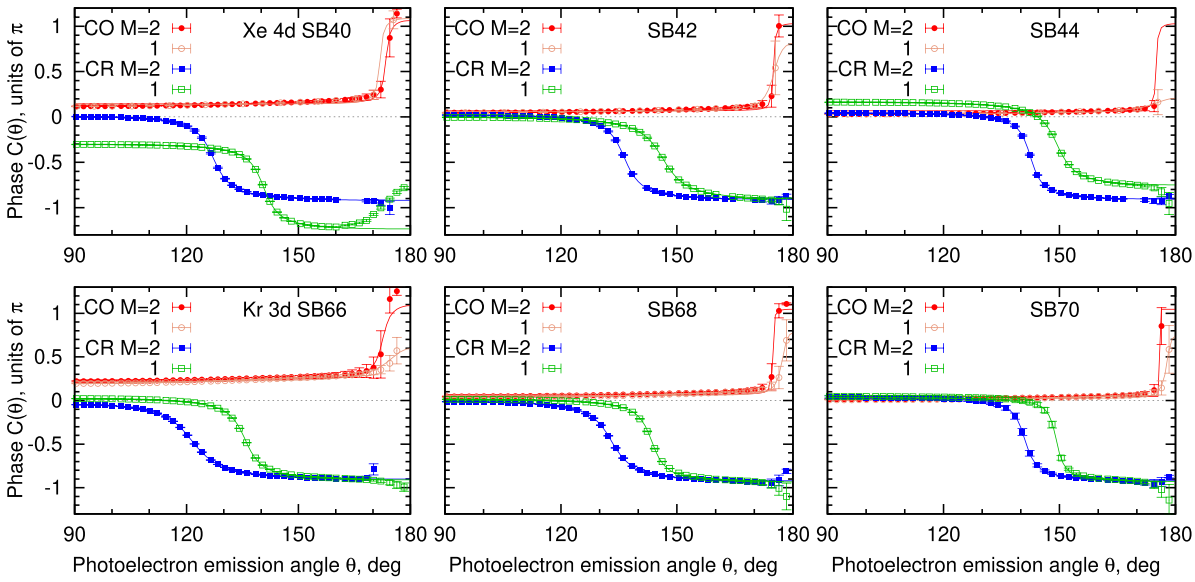

Figure 3. Angular dependent *c*RABBITT phase $C(\theta)$ in the lowest SB's of Xe 4*d* (top) and Kr 3*d* (bottom). The CO and CR $C(\theta)$ values are extracted from the $M = 1$ and $M = 2$ angular momentum projections. The raw values are shown with error bars of the cosine fit with equation (1). The solid lines of the matching color exhibit the angular fit with equation (11).

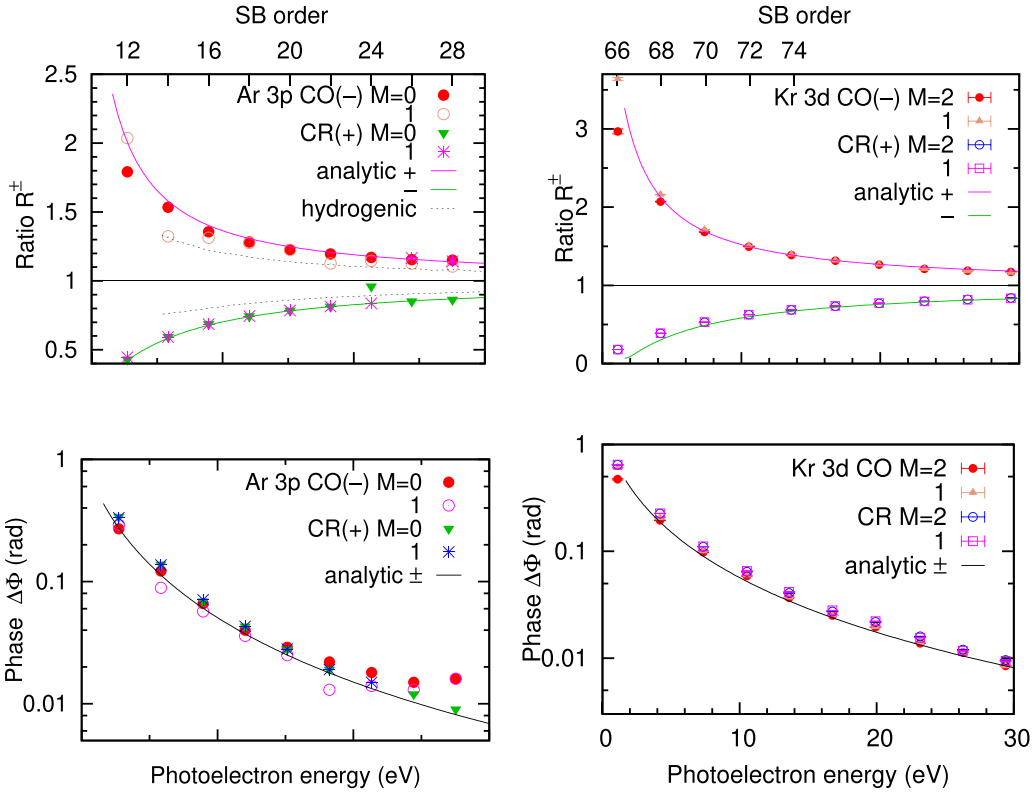

Figure 4. The *c*RABBITT amplitude ratios $R^{\pm}$ (top) and the relative phases $\Delta\Phi$ (bottom) in Ar 2*p* (left) and Kr 3*d* (right). The CO(–) and CR(+) ratios and phases are extracted from the $M = 0, 1$ projections for Ar and $M = 1, 2$ for Kr. The analytic predictions from [11] are shown with solid lines whereas the dotted lines visualize the hydrogenic values of [25].

for larger photoelectron energies where the relative phases are very small. At these energies, the two sets of CO and CR ratios tend to unity for both target atoms. At lower end of the photoelectron energy scale, the Xe 4*d* ratios deviate from unity markedly stronger than the same ratios for Ar 3*p* as predicted by the analytic model [11].

We observe in figure 4 that the amplitude ratios and relative phases are rather close for various M projections. Ideally, they should be identical. Thus a weak M dependence indicates the accuracy of our determination. In addition, the relative phases are almost the same in the CR and CO polarization cases.

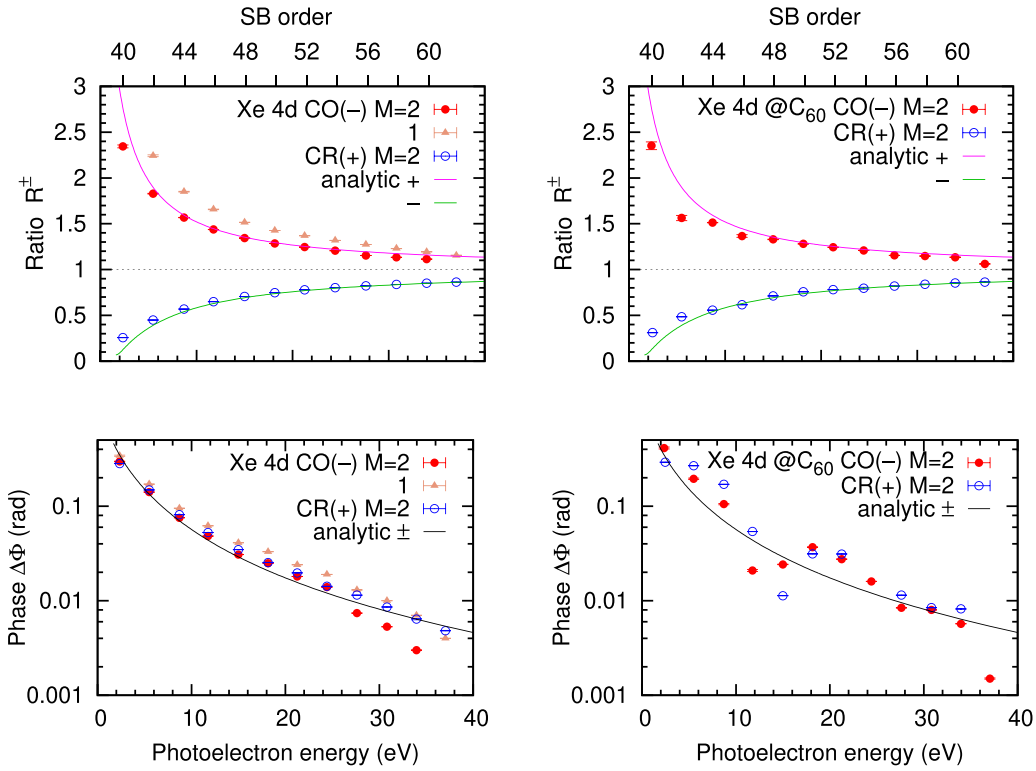

Figure 5. The *c*RABBITT amplitude ratios $R^{\pm}$ (top) and the relative phase $\Delta\Phi$ (bottom) in the free Xe 4*d* atom (left) and the same atom inside the C_{60} cage (right). The CO(–) and CR(+) ratios and phases are plotted in the $M = 2$ and $M = 1$ (where available) angular momentum projections. The analytic predictions for the ratios and phases are from [11].

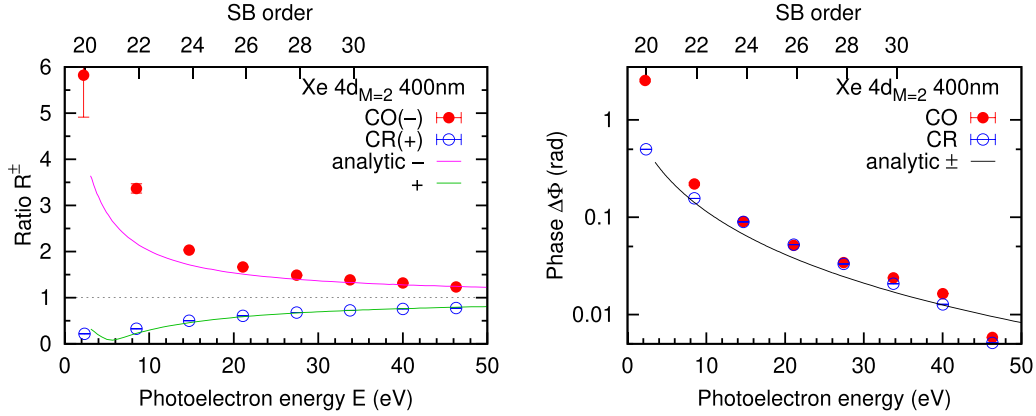

Figure 6. The *c*RABBITT amplitude ratios $R^{\pm}$ (top) and the relative phase $\Delta\Phi$ (bottom) in Xe 4*d* at the wavelength of 400 nm. The CO(–) and CR(+) ratios and phases are extracted from the $M = 2$ angular momentum projection. The analytic predictions for the ratios and phases are from [11].

We continue to exhibit our ratios and phases in figure 5 where we compare the 4*d* shell of the free Xe atom (left) and of the same atom trapped in the C_{60} cage (right). This trapping causes confinement resonances which manifest themselves in photoionization cross-section, angular anisotropy β parameter and time delay [14, 26]. In comparison to this set of data, the $R^{\pm}$ ratios and $\Delta\Phi$ phases are rather insensitive to the confinement. Except for a single data point in the R^{-} ratio, the bare Xe and Xe @C_{60} data are very similar. The relative phases $\Delta\Phi$ do show some oscillatory structure however the data points are too scattered to link this oscillation with any particular resonance.

Our next set of the ratios and phases is exhibited in figure 6 where we present the Xe 4*d* results with the IR wavelength halved to 400 nm. As predicted in [11], such a decrease should result in a stronger deviation of the amplitude ratios from unity. This deviation can be indeed observed in the left panel of Figure 6. Our numerical results follow the trend of the analytic model except for the lower end of the photoelectron energy scale. Here the CO ratio and phase are very

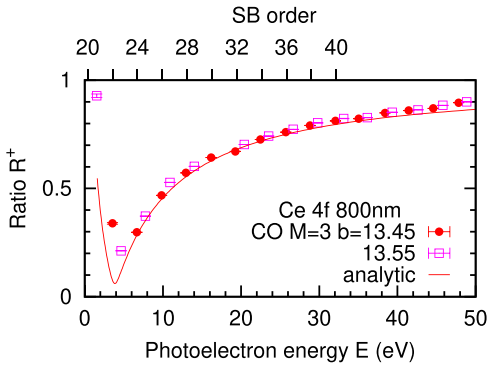

Figure 7. The *c*RABBITT amplitude ratio R^+ in Ce 4*f* at the wavelength of 800 nm. The CR(+) ratios are extracted from the $M = 3$ angular momentum projection. The two sets of data are shown with a slight modification of the LHG *b* parameter and the corresponding ionization potential. The analytic prediction is from [11].

large. We attribute this deviation from the analytic model to the crossing of the lowest harmonic peak H_{19} below the ionization threshold. Such a phenomenon which we term the under-threshold RABBITT or *u*RABBITT for brevity, allows to probe the discrete target states [27–29]. Under this condition, the continuous phase in one of the arms of the RABBITT interference should be substituted with the resonant phase. The same effect manifest itself in the *c*RABBITT where both the amplitude ratio and the relative phase are affected by the under-threshold resonance.

Our final set of results is presented in figure 7 where we exhibit the R^+ ratio in the 4*f* shell of the cerium atom. In this computations, the LHF potential (13) was used with $Z = 58, a = 4.16, b = 13.45$. Comparison with the analytic model [11] indeed confirms a formation of a Cooper-like minimum in the R^+ ratio. Because the said minimum is rather narrow and cannot be spanned by a limited number of SB's, an additional set of calculations was performed by adjusting the *b*-parameter to 13.55 which reduced the ionization potential by 2 eV. The two sets of the TDSE calculations hint to the presence of the Cooper minimum. However the ratio R^+ still remains below unity and the Fano propensity rule is not yet violated.

5. Summary and outlook

In this work, we examined the angular dependence of the RABBITT phase in cases where both XUV and IR ionization are driven by circularly polarized radiation. In a *c*RABBITT process, the strict selection of photoelectron angular momentum and its projection significantly restricts the accessible continuum states. This simplification reduces the complexity of the angular dependence of the *c*RABBITT phase, enabling the separation of radial matrix elements from the corresponding spherical harmonics. Consequently, the absolute ratios and relative phases of these matrix elements can be extracted from either numerical simulations or experimental data. Such an extraction was demonstrated for He 1*s* and Ar 3*p* in our previous work [7].

In this work, we extend our analysis to heavier targets, specifically Kr 3*d*, Xe 4*d* and Ce 4*f*. A larger number of the available orbital momentum projections in the initial state restricts experimental use of the proposed procedure. However, our numeric experimentation using the TDSE allows for an unambiguous extraction of the amplitude ratios and their relative phases. Such an extraction is motivated by predictions from a recently developed analytical model [11], which suggests that the deviation of the amplitude ratios from unity increases significantly as the angular momentum of the target orbital and the frequency of the IR photon rise. While we confirm these trends, we are unable to verify another important theoretical prediction: at sufficiently high photon frequencies and large orbital momentum, the Fano propensity rule for IR photon absorption is expected to be violated, causing the amplitude ratio $R^+ = \left|T^+_{\ell\to\ell-1}/T^+_{\ell\to\ell+1}\right|$ to exceed unity. This trend is predicted to coincide with the appearance of a 'Cooper-like' minimum in R^+. This minimum is indeed observed in the Ce 4*f* shell as shown figure 7.

Doubling the IR photon frequency as in the case of Xe 4*d* visualized in figure 6 does not reveal the Cooper minimum sufficiently clearly because the sideband separation by 2ω reduces the number of useful data points. Additionally, as the lowest harmonic peak crosses below the ionization threshold, the resulting ratios and phase differences are influenced by the *u*RABBITT process. Both of these challenges can potentially be addressed through attosecond streaking driven by circularly polarized XUV and IR pulses. Ionization driven by linearly polarized XUV radiation and streaked by circularly polarized IR pulses has already been achieved [30, 31], suggesting that extending this setup to circularly polarized XUV and IR pulses is feasible. This approach represents a promising direction for continuing the present work.

In conclusion, we want to highlight one of the central points of the present work. It is the separability of the XUV and IR ionization processes in *c*RABBITT. The XUV photon absorption elevates an electron from the initially bound state to the continuum. This process is very sensitive to the ionic potential as it takes place close to the origin. Hence, the XUV results of Kr 3*d* and Xe 4*d* differ so substantially. The subsequent IR photon dressing takes place in the continuum and hence it is much less sensitive to the ionic core potential which is asymptotically always hydrogenic. The results of the *c*RABBITT simulations contain the amplitude ratios and the phase differences. In such a construction, the XUV part of the two-photon ionization amplitude is factored out. The remaining IR part is rather insensitive to the target and compares well with the predictions of a hydrogenic model [11].

Data availability statement

All data that support the findings of this study are included within the article (and any supplementary files).

Acknowledgments

This investigation was inspired by discussions between the author and members of Prof. Hans Jakob Wörner's group at ETH Zürich, whose warm hospitality is gratefully acknowledged. The author also extends sincere thanks to Dr JiaBao Ji and Prof. Kiyoshi Ueda for their invaluable input; special acknowledgment goes to Dr Ji for generously providing his data in numerical form. The author is grateful to his former PhD student, Dr Alexander Bray, for his assistance with the TDSE computer code. This research heavily relied on the computational resources of the National Computational Infrastructure facility, provided under the Australian National University Merit Allocation Scheme.

ORCID iD

Anatoli S Kheifets https://orcid.org/0000-0001-8318-9408

References

[1] Klünder K *et al* 2011 Probing single-photon ionization on the attosecond time scale *Phys. Rev. Lett.* **106** 143002
[2] Dahlström J, Guénot D, Klünder K, Gisselbrecht M, Mauritsson J, Huillier A L, Maquet A and Taïeb R 2012 Theory of attosecond delays in laser-assisted photoionization *Chem. Phys.* **414** 53–64
[3] Donsa S, Douguet N, Burgdörfer J, Brezinová I and Argenti L 2019 Circular holographic ionization-phase meter *Phys. Rev. Lett.* **123** 133203
[4] Han M, Ji J B, Balciunas T, Ueda K and Wörner H J 2023 Attosecond circular-dichroism chronoscopy of electron vortices *Nat. Phys.* **19** 230–6
[5] Han M, Ji J B, Ueda K and Wörner H J 2023 Attosecond metrology in circular polarization *Optica* **10** 1044–52
[6] Han M, Ji J B, Leung C S, Ueda K and Wörner H J 2024 Separation of photoionization and measurement-induced delays *Sci. Adv.* **10** eadj2629
[7] Kheifets A S 2024 Characterization of XUV+IR ionization using the circular dichroic phase *Phys. Rev. Res.* **6** L012002
[8] Busto D *et al* 2019 Fano's propensity rule in angle-resolved attosecond pump-probe photoionization *Phys. Rev. Lett.* **123** 133201
[9] Maquet A and Taïeb R 2007 Two-colour IR+XUV spectroscopies: the soft-photon approximation *J. Mod. Opt.* **54** 1847–57
[10] Berkane M, Lévêque C, Taïeb R, Caillat J and Dubois J 2024 Probing wigner time delays with photoelectron interferometry: anisotropic long-range imprint of the short-range centrifugal potential *Phys. Rev.* A **110** 013120
[11] Ji J B, Ueda K, Han M and Wörner H J 2024 Analytical expression for continuum-continuum transition amplitude of hydrogen-like atoms with angular-momentum dependence *J. Phys.* B **57** 235601
[12] Ivanov I A and Kheifets A S 2017 Angle-dependent time delay in two-color XUV+IR photoemission of He and Ne *Phys. Rev.* A **96** 013408
[13] Bray A W, Naseem F and Kheifets A S 2018 Simulation of angular-resolved RABBITT measurements in noble-gas atoms *Phys Rev.* A **97** 063404
[14] Bray A W, Naseem F and Kheifets A S 2018 Photoionization of Xe and Xe@C_{60} from the 4*d* shell in RABBITT fields *Phys. Rev.* A **98** 043427
[15] Patchkovskii S and Muller H 2016 Simple, accurate and efficient implementation of 1-electron atomic time-dependent Schrödinger equation in spherical coordinates *Comput. Phys. Commun.* **199** 153–69
[16] Tao L and Scrinzi A 2012 Photo-electron momentum spectra from minimal volumes: the time-dependent surface flux method *New J. Phys.* **14** 013021
[17] Morales F, Bredtmann T and Patchkovskii S 2016 iSURF: a family of infinite-time surface flux methods *J. Phys.* B **49** 245001
[18] Strohmaier E, Dongarra J and Simon H many others 2024 The 500 Most powerful commercially available computer systems (available at: https://top500.org/site/47369/)
[19] Sörngard J, Dahlström J M and Lindroth E 2020 Study of the possibilities with combinations of circularly and linearly polarized light for attosecond delay investigations *J. Phys.* B **53** 134003
[20] Williams T and Kelley C many others 2014 Gnuplot 4.6: an interactive plotting program (available at: http://gnuplot.sourceforge.net/)
[21] Toffoli D, Stener M and Decleva P 2002 Application of the relativistic time-dependent density functional theory to the photoionization of xenon *J. Phys.* B **35** 1275
[22] Sarsa A, Gálvez F J and Buendia E 2004 Parameterized optimized effective potential for the ground state of the atoms He through Xe *At. Data Nucl. Data tables* **88** 163–202
[23] Wendin G and Starace A F 1978 Perturbation theory in a strong-interaction regime with application to 4D-subshell spectra of Ba and La *J. Phys.* B **11** 4119
[24] Kheifets A S 2013 Time delay in valence-shell photoionization of noble-gas atoms *Phys. Rev.* A **87** 063404
[25] Boll D I R, Martini L, Palacios A and Fojón O A 2023 Two-color polarization control of angularly resolved attosecond time delays *Phys. Rev.* A **107** 043113
[26] Mandal A, Deshmukh P C, Kheifets A S, Dolmatov V K and Manson S T 2017 Angle-resolved Wigner time delay in atomic photoionization: The 4*d* subshell of free and confined Xe *Phys. Rev.* A **96** 053407
[27] Kheifets A S and Bray A W 2021 RABBITT phase transition across the ionization threshold *Phys. Rev.* A **103** L011101
[28] Kheifets A S 2023 Under-threshold RABBITT in argon *J. Phys.* B **56** 095201
[29] Kheifets A 2021 Revealing the target electronic structure with under-threshold RABBITT *Atoms* **9** 66
[30] Kheifets A S, Wielian R, Serov V V, Ivanov I A, Wang A L, Marinelli A and Cryan J P 2022 Ionization phase retrieval by angular streaking from random shots of XUV radiation *Phys. Rev.* A **106** 033106
[31] Driver T *et al* 2024 Attosecond delays in x-ray molecular ionization *Nature* **632** 762–7